ORIGINAL PAPER

Cellulose-Based Hybrid Composites Enabled by Metal Organic Frameworks for CO$_2$ Capture: The Effect of Cellulosic Substrate

Saysam Qusai Jabbar[1] · Halimeh Janani[1] · Hamed Janani[1]

Abstract

A comparative study of two cellulosic materials i.e., cotton fabrics and bacterial cellulose nanofibers (NBC), is reported as substrates for metal organic frameworks (MOF-199), to prepare micro and nanocomposites of cellulose@MOF-199 for CO$_2$ capture. The CO$_2$ uptake performance was investigated using gravimetric adsorption and desorption kinetics. NBC was an efficient substrate with full coverage and uniform distribution of MOF crystals observed in NBC@MOF-199 nanocomposite. The surface area for NBC@MOF-199 and Cotton@MOF-199 were 553.4 m^2 g^{-1} and 168.9 m^2 g^{-1}, respectively. NBC@MOF-199 showed a high adsorption capacity (2.9 mmol g^{-1}) at ambient temperature and pressure, followed by Cotton@MOF-199 (1.2 mmol g^{-1}). The kinetic studies revealed that the adsorption process is controlled by film diffusion at lower temperatures, and by sorption to active sites at higher temperatures. The estimated thermodynamic parameters represent a spontaneous adsorption with low activation energies of adsorption/desorption, promising a fast adsorption and facilitated regeneration adsorbent system with minimum energy costs.

Keywords Bacterial cellulose nanofibers · Cellulose-MOF composites · CO$_2$ capture · Adsorption kinetics

Introduction

The ever-increasing atmospheric concentrations of the greenhouse gases, particularly CO$_2$, is an environmental issue that requires developing technologies to restrict its emissions. Adsorption is a promising technique for CO$_2$ capture, since it is a cost effective, low energy demanding, and environmentally friendly technology. In this regard, metal organic frameworks (MOFs) have been considered as CO$_2$ adsorbent due to their tunable micro-/mesoporous structure, chemical functionality, and high surface areas [1–4]. However, MOFs are usually produced as powder or colloid crystals, and forming them into monoliths is a challenge which hinders their practical application, particularly when structural integrity is needed, e g. for gas adsorptive masks and filters [5]. One approach for production of such desirable MOF 3D architecture is to grow the MOF crystals on the surface of a substrate [6–9] to shape them into mechanically durable forms.

Natural polymers, such as cellulose, in addition to renewability, biodegradability, and low cost, usually show adequate mechanical strength and porosity to be used as a substrate for MOF crystals [10–17]. A hybrid of cellulose@MOF has the durability of the cellulosic substrate along with a high surface area and adsorption capacity of MOFs [18]. Multiple functionalities have been recognized for this important class of green materials, such as antibacterial composite fabrics (due to the presence of metal ions such as copper, zinc and silver in the structure of MOF) [17, 19], wastewater treatment [20, 21], air purification [22], medical applications [23, 24] and CO$_2$ adsorption [25, 26]. Comprehensive reviews have been recently published on the hybrid cellulose–metal organic frameworks (CelloMOFs) [25], cellulose-zeolitic imidazolate frameworks (CelloZIFs) [26], and their particular applications to solve environmental issues.

Cellulose in various forms have been used in the construction of cellulose@MOF [14, 27–30]. The structural features and availability of a cellulosic substrate depends on its source of extraction. Bacterial cellulose, for example, is inherently composed of a network of cellulosic nanofibers, which offer a very high porosity compared to conventional

✉ Hamed Janani
 janani@um.ac.ir

1 Chemical Engineering Department, Faculty of Engineering, Ferdowsi University of Mashhad, Azadi Sq., Mashhad 9177948944, Iran

plant-based cellulose, but its large-scale production is costly. Cotton, on the other hand, has a multilayer microfiber structure, and it is one of the most abundant plant sources of cellulose, readily available at a low price for use in the production of masks and filter media. Ma et al. used bacterial cellulose nanofibers as a template for amino-functionalized ZIF-8 (NH$_2$-ZIF-8) and reported a high CO$_2$ adsorption capacity of 1.63 mmol g^{-1} at 25 °C and 1 bar [31]. Wang et al. studied a TEMPO-oxidized wood (TO-wood) template for three types of MOFs [32]. They reported that the TO-wood/Cu$_3$(BTC)$_2$ presents a mechanically robust composite with a high specific surface area of 471 m^2 g^{-1} and a high CO$_2$ adsorption capacity of 1.46 mmol g^{-1} at 25 °C and atmospheric pressure [32]. Other forms of cellulose that have been used to manufacture cellulose@MOF composites include cellulose nanofiber (CNF) [14, 27], cellulose nanocrystals (CNC) [28], and cellulose acetate (CA) [29, 30].

The morphological characteristics of the cellulosic substrate could significantly affect the adsorption behavior of this class of composites. A comparative study of cellulosic materials with different structural features for their performance as substrate for MOFs is interesting because most of previous studies have been focused on one form of cellulose as substrate with various MOFs. The present study aims to use cotton fabric and NBC, as substrates for MOF powders, and to investigate the CO$_2$ adsorption performance of the developed cellulose-MOF composite. Potential applications for these composites would be as CO$_2$ capture filters, antibacterial/gas adsorptive medical masks/clothing, and air purifying filters. As there is a lack of reports on the effect of cellulosic substrate on the CO$_2$ capture performance of cellulose@MOF-199 composites, and particularly on the kinetic and thermodynamic characteristics of such systems, this work contributes to advancing the knowledge on structure-adsorption relations of these composites.

The MOF-199 (also known as HKUST-1), extensively studied for CO$_2$ adsorption [33–37], is used here to prepare the cellulose@MOF composites. This MOF is formed by the association of Cu^{2+} cations with benzene-1,3,5-tricarboxylic acid as a ligand (Cu$_3$BTC$_2$). MOF-199 possesses high porosity and ultrahigh surface area, reported in the range of 692 to 1510 m^2 g^{-1} in different studies [33]. It is a commercially available MOF with a relatively simple production route. The coordinatively unsaturated cupper centers in the MOF-199 structure provide suitable active sites for CO$_2$ adsorption [33–35]. CO$_2$ uptake capacities in the range of 4 [36] to 13 mmol g^{-1} [37], at ambient temperature and pressures from 1 to 15 bar, have been reported for pure MOF-199. The approach, used in this research, to elucidate the adsorption mechanism in the composite of the MOF with the naturally occurring polymers includes investigation of various well-known gas adsorption kinetic models to see which ones best describe the experimental adsorption data of biopolymer-MOF composites. Finally, we report here an antibacterial green adsorbent system with a relatively high CO$_2$ uptake capacity, fast adsorption, and facilitated regeneration favoring minimum energy costs of CO$_2$ capture.

Materials and Methods

Materials

The Bacterial cellulose nanofiber (NBC) sheet (purity: ≥ 99%, solvent: deionized water, average size: 30–50 nm, source: bacterial synthesis) was purchased from Nano Novin Polymer, Iran. The copper (II) nitrate trihydrate, trimesic acid, sodium chloroacetate, and N,N-dimethylformamide (DMF) were obtained from E. Merck, Germany. Sodium hydroxide, ethanol (EtOH), and deionized water were purchased from Mojallali chemicals, Iran.

Cellulose@MOF Composite Preparation Procedure

bacterial cellulose nanofibers and cotton fabric swatches with dimensions 5 cm × 5 cm were used to prepare the bacterial cellulose-MOF-199 (NBC@MOF-199) and Cotton@MOF-199 composite. The post-synthetic modification (PSM) approach, as described by Lange et al. [38], was used to prepare the composites.

The procedure includes three major steps: an esterification modification to obtain carboxymethylated cellulose (1st step) to create anionic sites on cellulosic substrate for subsequent bonding with Cu ions during the nucleation of MOF (2nd step), followed by the MOF crystal growth in trimesic acid solution (3rd step) as shown in Scheme 1. The details of composite preparation are described in the following sections.

Carboxymethylation of Cellulosic Substrates

In order to enhance bonding between the substrate and the MOF, an esterification reaction was performed with the appendant hydroxyl groups of the cellulose sheets to insert carboxylate functional groups on the surface. The anionic carboxylate sites chelate with the Cu ions and start the nucleation and growth of the MOF crystals. In a typical carboxymethylation procedure [38], the swatches were soaked in an aqueous solution of 30 g sodium hydroxide in 150 mL deionized water for 10 min. The specimens were removed, patted dry, heated to 45 °C for 10 min, and soaked/stirred in 150 mL dionized water containing sodium chloroacetate (30 g) for one more hour. The specimens were again patted dry and heated in a preheated oven at 85 °C for 30 min. The resulting samples were washed with 100 mL deionized water
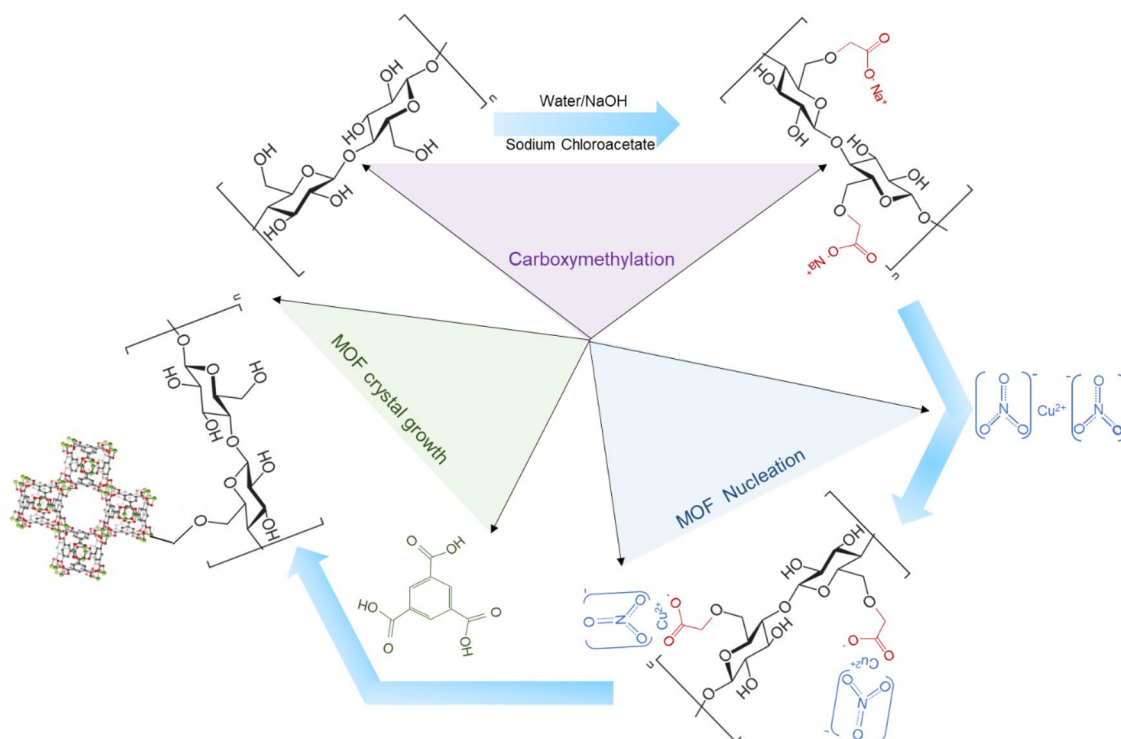
Scheme 1 Schematic of the process to carboxymethylate and grow the MOF-199 on the surface of bacterial cellulose nanofibers

three times, and acidified with 150 mL of a 2 g/L acetic acid solution for 5 min. Washing procedure with deionized water was repeated, and the samples were finally dried in an open atmosphere.

Nucleation and Growth of MOF-199 on Cellulosic Substrate

The second step is the assembly of the MOF-199 structure on the modified bacterial cellulose swatches. It was done by repetitive and sequential dipping the carboxymethylated bacterial cellulose (C-NBC) swatches into separately prepared copper and ligand-containing solutions. A 20 mL mixture of 1:1 deionized water and ethanol containing 1.90 g copper (II) nitrate was used as solution A, and solution B was the same solvent mixture with 1 g of trimesic acid. Complete dissolution of the components was assured by proper mixing for sufficient time (30 min) followed by sonication for 20 min.

The carboxymethylated cellulosic specimens were dipped first in solution A by stirring at room temperature for 30 min. Then it was removed, and transferred to methanol beaker for 30 s, followed by dipping in trimesic acid solution (solution B) under magnetic stirring for 30 min. The cycle was repeated 17 times. The as-synthesized composites were removed from the reaction vessel and stirred in 50 mL of deionized water for 1 h, followed by 50 mL of DMF for 1 h, and finally 50 mL ethanol for another hour to

remove MOF-199 and any unreacted chemicals that are not attached chemically to the cellulosic substrate. The modified specimens were then vacuum dried overnight at room temperature. The composite is labeled NBC@MOF-199.

For comparative studies, the same procedure as described above was performed using cotton fabrics instead of bacterial cellulose. The prepared carboxymethylated cellulose and MOF-cellulose composites are labeled C-cotton and Cotton@MOF-199, respectively. All the prepared composites have blue color, as shown in Fig. 1 for NBC@MOF-199.
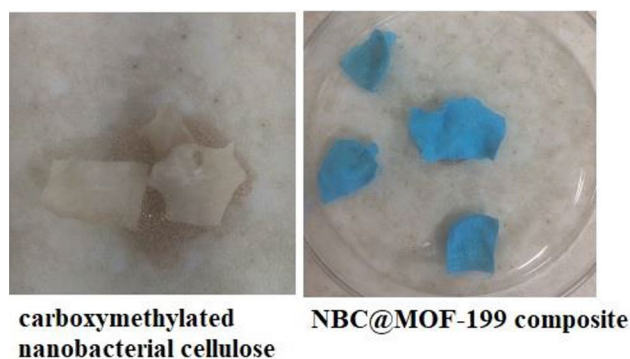

carboxymethylated
nanobacterial cellulose

NBC@MOF-199 composite

Fig. 1 Optical images of carboxymethylated NBC (left) and NBC@MOF-199 (right)

Characterizations

FT-IR spectra were recorded using Thermo Nicolet AVA-TAR 370 FT-IR spectrometer with KBr pellets. X-ray diffraction (XRD) measurements were performed on a Theta/Theta XRD-Explorer X-Ray Diffractometer (GNR, Italy) with Cu kα radiation. This device works with an accelerating voltage of 40 kV and a current of 30 mA, emitting a wavelength of 1.54 Å. The X-ray diffraction pattern was recorded in 2θ angle range of 5–25°.

Leo 1450 Vp scanning electron microscopy (Carl Zeiss, Germany) was used to study the morphology of composites and to examine the changes in the cellulose tissue before and after MOF fixation on the cellulose. The SEM samples' surfaces were sputtered and coated with gold using a sputter coater SC7620 (Quorum Technologies, UK).

BELSORP MINI II (BEL, Japan) was used to measure the nitrogen adsorption/desorption curves, BET surface area, and pore size. The samples were cut into tiny pieces or powdered. Sample preparation involves drying and degassing at 120° C under vacuum for 2 h using BEL PREP VAC II (BEL, Japan).

The kinetic adsorption tests were performed using a thermogravimetric analyzer (SDTQ600, TA Instruments) at atmospheric pressure and three temperatures, including 25, 45 and 65 °C. A constant gas flow (1 atm, 40 mL min^{-1}) of highly pure CO_2 (99.99% pure) was used as the adsorbate gas stream. For each adsorption test, a sample of about 20 mg was loaded into an alumina pan. To remove the pre-adsorbed species, such as atmospheric CO_2, water, and other volatiles, the samples were degassed at 120 °C for 60 min using pure N_2 stream at flow rate of 50 mL/min. The sample temperature was allowed to cool down to the desired adsorption temperature, and meanwhile, the gas stream was switched from pure N_2 to pure CO_2 with the flow rate set at 40 mL/min. The CO_2 uptake was followed for 20 min. After equilibration, the gas stream was switched again to pure N_2 at 50 mL/min, while the temperature was raised to 90 °C, and the desorption at constant temperature was followed for 30 min. The CO_2 adsorption in mmol g^{-1} was calculated from the mass of adsorbent at time t and the initial mass of the sample. Since the gas pressure and flow rate is low, the buoyancy and drag effects are neglected [39].

Results and Discussion

Synthesis and Structural Characterization

FTIR spectra of the original cotton fabric and NBC, as well as C-cotton and C-NBC were obtained in order to investigate the successful substitution of hydroxyl groups by carboxymethylation (Fig. 2). In the spectra of C-NBC, the appearance of a peak at 1730 cm^{-1} (vertical line) is associated with the C=O bond stretch in the carboxylate group. In addition, the intensity of the peak at 3415 cm^{-1}, corresponding to OH stretch, decreases in C-NBC compared to NBC, presenting the successful substitution of hydroxyl groups with carboxylate.

Similarly, the characteristic peak at 1710 cm^{-1} of the C=O bond stretch is observed in spectra of C-cotton. It has been explained that the intensity of peak associated with the C=O bond stretch in carboxymethylated cellulose is proportional to the degree of modification (degree of carboxylate substitution) [40]. Comparing the intensity (area under the peak) associated with C=O stretching in C-cotton and C-NBC, it is clear that the peak of C-cotton is less intensive. It can be concluded that a higher degree of substitution is obtained by chemical modification in the case of C-NBC. The more exposed surface area of NBC due to its

Fig. 2 FT-IR spectra of non-treated bacterial cellulose nanofibers (NBC) and cotton fabric (black curve), in comparison with carboxymethylated bacterial cellulose (C-NBC) and cotton (C-cotton)
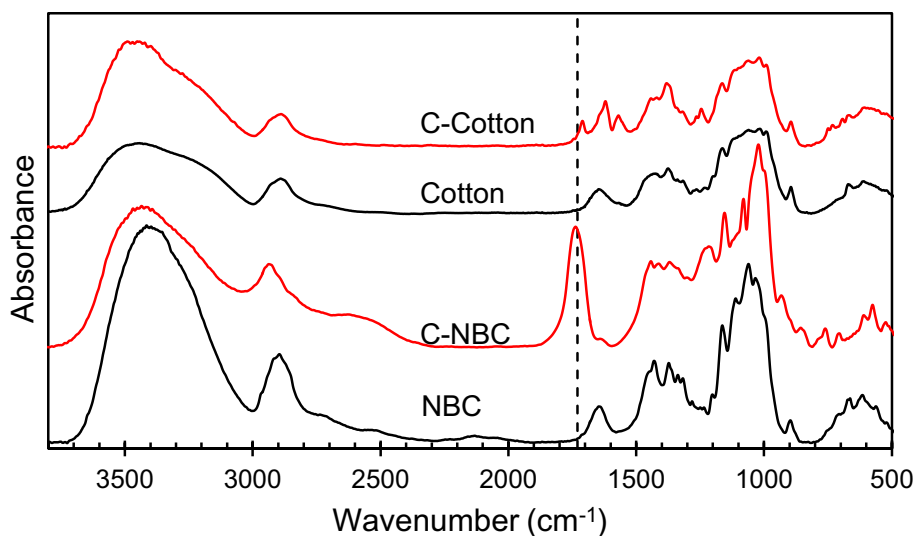
nanofibrous network structure, results in more effective substitution reaction. As mentioned in the experimental section, the substituted carboxylate groups act as nucleation sites on cellulose fiber to grow MOF-199 crystals, hence, higher area density of nucleation sites shall be available on C-NBC.

In order to prove the formation of MOF crystals on the cellulosic substrates the crystallographic structure of the composites was examined by XRD. The X-ray diffractograms of native bacterial cellulose, MOF-199 powder, NBC@MOF-199, and Cotton@MOF-199 composites are presented in Fig. 3. All the graphs are normalized (intensity divided by total area under the curve) to have an area under the curve equal to one. The diffraction peaks of NBC appear at $2\theta =$ 14.3°, 16.7°, and 22.5°, characteristic of Cellulose I crystal structure [41]. A similar pattern was observed for the carboxymethylated NBC, confirming that the chemical and solvent treatments during the composite production process did not affect the polymorphic behavior of the crystalline NBC. The crystal structure of MOF-199 is characterized by an octahedral shape 3D structure with characteristic peaks at $2\theta =$ 6.9°, 9.5°, 11.6°, 13.4°, 17.5°, 19°, 26°, and 29.3° [42]. The diffractogram of the NBC@MOF-199 composite represents all the characteristic peaks related to the MOF-199. Particularly, peaks of MOF at 6.9°, 9.5°, and 11.6° do not overlap with cellulose crystal peaks. Hence, they can be helpful in proving the formation of MOF on NBC surface. It can be seen that the crystallographic features of the C-NBC and the MOF-199 are preserved after treatment (Fig. 3). The existence of the MOF crystals in Cotton@MOF-199 composites is also confirmed by the relevant diffraction peaks of MOF-199 observed clearly in the diffractogram of this sample. However, the diffraction
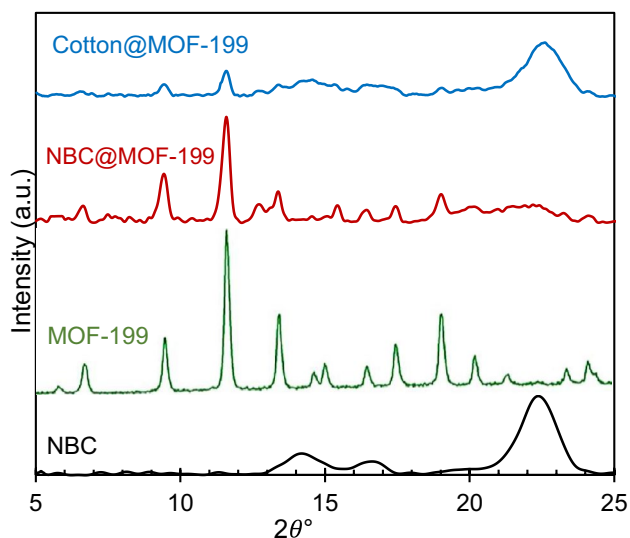
peaks are relatively less intensive as compared to the NBC@MOF-199 pattern. Since all the patterns are normalized, the relative intensity could be considered as the lower amounts of MOF crystals in Cotton@MOF-199.

The surface coverage of the MOF onto NBC swatches and cotton fabrics was investigated using SEM. Figure 4a and b compare the morphology of the primary NBC and the chemically modified C-NBC. The structure of primary NBC intrinsically consists of a network of nanofibers with an average diameter of about 40 nm (Fig. 4a). After chemical modification, a significant agglomeration of nanofibers occurs, as is observed in Fig. 4b. The average fiber diameter in C-NBC is about 450 nm, more than ten times the original bacterial cellulose. The treatment of NBC with chemical solutions and subsequent drying in the atmosphere causes this significant agglomeration of nanofibers.

The microstructures of the developed composites, NBC@MOF-199 and Cotton@MOF-199, are also shown in Fig. 4 at two different magnifications. A full coverage of the NBC surface by the grown MOF microcrystals is observed in NBC@MOF-199 composites (Fig. 4c and d). The MOF crystals are evenly distributed on the surface. It can be concluded that there were plenty of nucleation sites available at the surface of the C-NBC for MOF crystals to grow. The MOF crystallites on NBC appear to be approximately 3–5 μm in diameter with little twinning of the crystallites. Hence, little agglomeration occurred due to the growth of MOF crystals on NBC substrate, and the dispersion is also acceptable. In conclusion, electron microscope images show that the products prepared with MOF-199 crystals are coated with homogeneous sizes and shapes, confirming the successful synthesis of the desired composites.

In the case of Cotton@MOF-199 composites, even distribution of MOF crystals on the fabric surface is observed in Fig. 4e and d. However, the cellulose fibers are not entirely covered by MOF crystals in this composite. Obviously, in the case of carboxymethylated cotton fabrics, there were less favorable nucleation sites (cellulose with grafted carboxylate moieties) available for MOF crystals to grow on it. The FTIR results are in agreement with this observation, since the peak associated with C=O stretching (the sign of the presence of carboxylate groups) was significantly more intense in the case of C-NBC as compared with C-cotton. The size of MOF crystallites, however, are a little smaller in Cotton@MOF-199 composites, (between 1 to 3 μm), presenting a better dispersion.

Adsorption Analysis

N$_2$ Adsorption–Desorption Isotherms

The isotherms were collected at 77 K. The samples were initially outgassed under vacuum for 2 h at 120 °C. The

Fig. 3 XRD patterns of NBC, pure MOF-199, NBC@MOF-199, and Cotton@MOF-199 composite. The graphs are normalized to have the area of 1
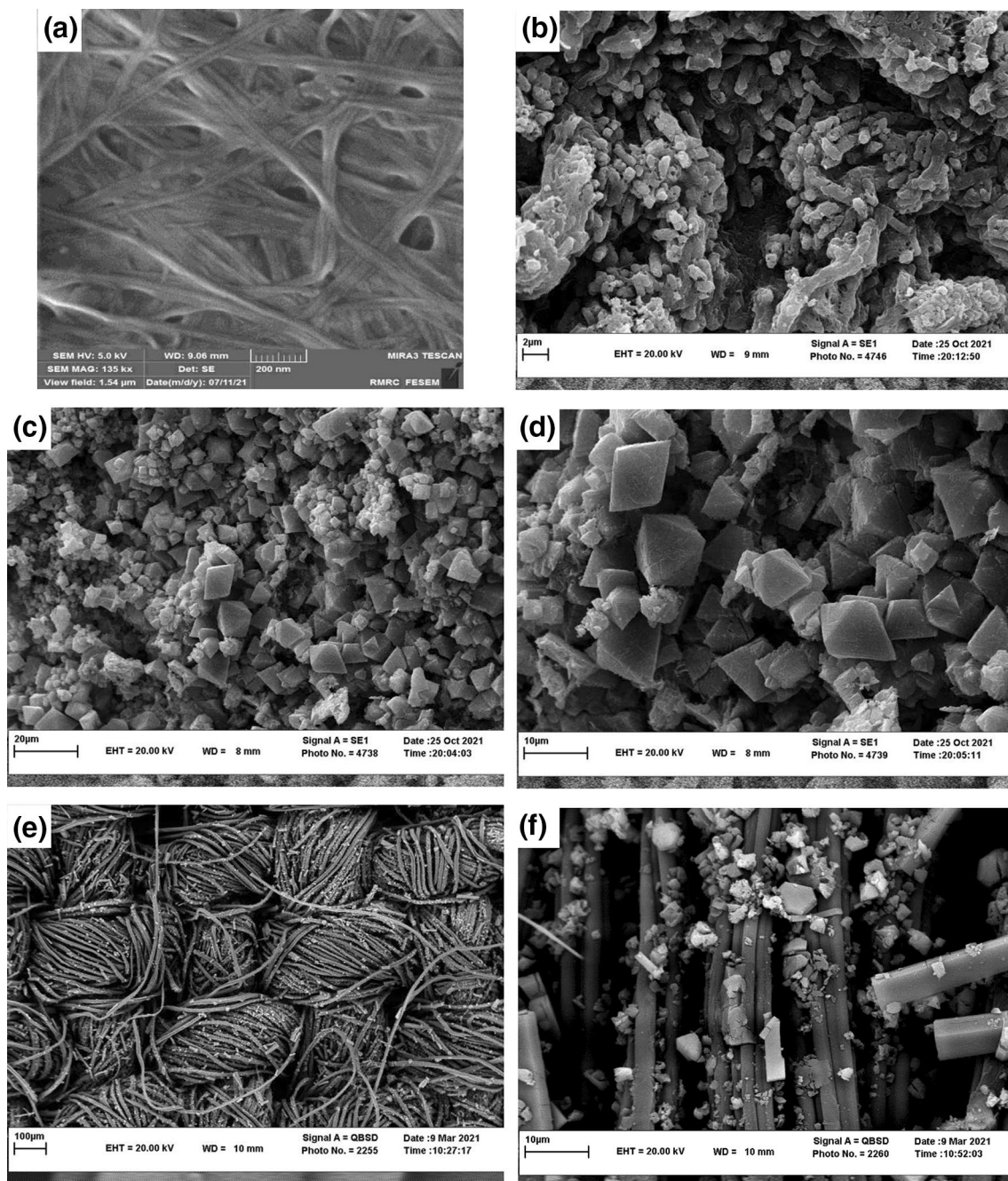
Fig. 4 SEM images of **a** the natural bacterial cellulose nanofibers (image magnification: 135 kX), **b** carboxymethylated bacterial cellulose (image magnification: 10 kX). Micrographs of NBC@MOF-199 surface at two magnifications **c** 2.5 kX and **d** 5 kX. SEM micrographs of Cotton@MOF-199 surface at two magnifications **e** 500 X and **f** 5 kX

resulting isotherms for C-cotton, C-NBC, and the composites are shown in Fig. 5. The sample surface area, total pore volume, and mean pore size were calculated using the BET analysis and presented in Table 1.

The C-cotton and C-NBC show a Type V isotherm with negligible H1 type hysteresis (Fig. 5a), representing weak interactions between adsorbate and the adsorbent. A very low surface area of ~ 3.6 $m^2 g^{-1}$ was estimated for C-cotton

from BET analysis. The C-NBC shows a higher surface area (a_{BET}~44 $m^2 g^{-1}$) and pore volume of ~ 0.082 $cm^3 g^{-1}$ (Table 1), but the isotherm similarly presents weak interactions (Fig. 5a).

The BET surface area for bacterial cellulose has been reported in the range of 25 to 65 $m^2 g^{-1}$ [43, 44] which is due to the network of nanofibrous structure and depends strongly on the drying procedure of NBC [43]. The reduction in

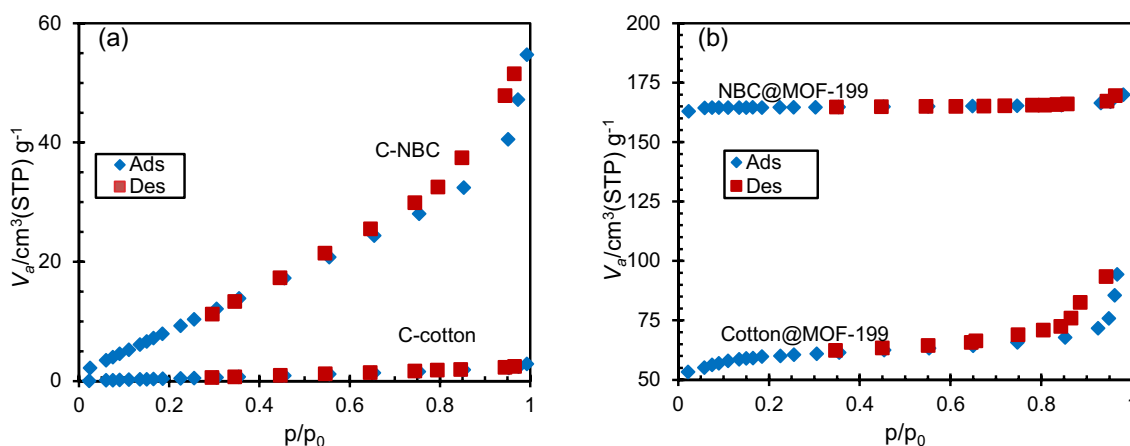**Fig. 5** N$_2$ adsorption/desorption plots for **a** C-NBC, C-cotton, and **b** NBC@MOF-199, C-cotton@MOF-199

Table 1 BET model parameters and pore structure analysis of the samples

	BET model parameters				Porosity characteristics		
	Slope (Linear)	Intercept (Linear)	^{a} V$_m$	C	^{b} a$_{BET}$	^{c} Total pore volume	^{d} Pore radius
C-cotton	0.713	0.496	0.83	2.4	3.6	0.004	4.9
C-NBC	0.085	0.013	10.2	7.5	44.4	0.085	7.6
Cotton@MOF-199	0.026	8E-5	38.8	322.2	168.9	0.146	3.5
NBC@MOF-199	0.019	0.0001	51.8	112.4	553.4	0.263	1.9

^{a} Unit: [cm^3 (STP) g^{-1}].

^{b} Unit: [m^2 g^{-1}].

^{c} Estimated at (p/p$_0$ = 0.99), Unit: [cm^3 g^{-1}].

^{d} Unit: nm

surface area after chemical modification of bacterial cellulose has been observed in previous reports [44]. For example, the phosphorylation of bacterial cellulose resulted in a reduction in specific surface area from 27.3 to 19.2 m^2 g^{-1} [44]. It seems that the network of cellulose nanofibers collapsed due to the interaction of cellulosic nanofibers with solvents and other reactants in the course of chemical treatment. The change in the microstructure of NBC after carboxymethylation is reflected in the SEM micrographs of NBC and C-NBC samples shown in Fig. 4a and b. The average fiber diameter increased from about 40 nm in the NBC sample to about 450 nm in the C-NBC sample, which clearly shows severe agglomeration of nanofibers after chemical treatment. Hence, the surface area and pore volume of the low surface area of original bacterial cellulose is expected to be even higher than the estimated values for C-NBC.

The N$_2$ adsorption isotherm of the Cotton@MOF-199 shows a composite Type IV + Type II isotherm (Fig. 5b) in which an inflection point is observed at a low relative pressure of P/P$_0$ < 0.1 but the isotherm does not level off at high relative pressure (as it is expected for a pure Type IV

behavior). The inflection point characterizes the presence of mesoporous structure, and the fact that the isotherm does not level off at high relative pressure could be due to the co-existence of macropores in the structure of Cotton@MOF-199 composite [45]. The macropores (pore size > 50 nm) are associated with the structure of the modified cotton substrate, and the micropores (pore size 2–50 nm) are essential to the MOF crystals. In other words, both macro and microporous structures play a role in gas adsorption to this composite.

The N$_2$ adsorption isotherm of NBC@MOF-199 (Fig. 5b) show completely different behavior compared to Cotton@MOF-199 composites, and it is more representative of Type I isotherm for microporous solid with the limited external surface [45]. In their study of pure MOF powders, Chowdhury et al. reported a type I behavior for HKUST-1 [36]. It seems that the microporous MOF-199 plays the main role in the adsorption in NBC@MOF-199 composites, and accounts for the negligible hysteresis observed in the desorption curve of NBC@MOF-199 compared to the higher hysteresis observed in the Cotton@MOF-199 composite.

According to the BET analysis, the specific surface area and the pore volume in the NBC@MOF-199 composite are 553.4 $m^2\,g^{-1}$ and 0.263 $cm^3\,g^{-1}$, respectively, and for the Cotton@MOF-199 are 168.9 $m^2\,g^{-1}$ and 0.146 $cm^3\,g^{-1}$, respectively (Table 1). Comparing these values with the specific surface area of C-cotton and C-NBC (3.6 $m^2\,g^{-1}$ and 44.4 $m^2\,g^{-1}$, respectively) shows a significant enhancement. The enhanced pore volume of the composites relative to the original cellulosic materials resulted from the high surface area provided by the microporous structure of the MOF.

A similar argument applies for the enhanced adsorption/desorption behavior of the composite NBC@MOF-199 compared to the Cotton@MOF-199. The difference in N_2 adsorption/desorption behavior of the samples must be related to their different macro and microscopic structure. As it was seen in Fig. 4, the SEM micrographs show higher MOF coverage of NBC fibers compared to the cotton fibers. It seems that there was higher density of nucleation sites available in NBC fiber surface for the growth of MOF crystals as compared to cotton fabric surface due to the higher level of carboxymethylation (FTIR results). The NBC is characterized by a high level of crystallinity made of a network of interconnected nanofibers. The morphology of NBC results in the high surface area available for successful growth of MOF crystals on the surface. Hence, the higher area and pore volume in NBC@MOF-199 composite as compared to Cotton@MOF-199.

These results show that using the NBC as the template in NBC@MOF-199 nanocomposites, in addition to enhancing the mechanical stability, provides a material with good porosity and hierarchical structure. In order to compare the porous structure of the adsorbents studied here, a pore size distribution was calculated by the Barrett−Joyner−Halenda (BJH) method, based on N_2 desorption isotherms (Fig. 6) for the composites and C-NBC. The NBC@MOF-199 composite shows a narrower pore size structure with two distinct peaks at ~ 4.6 and ~ 16 nm which are characteristic of the MOF structure. In the Cotton@MOF-199 composite, peaks are broader and less distinctive, which could be due to lower MOF coverage on cotton fibers, as observed in SEM micrographs of Fig. 4.

Kinetics of CO_2 Adsorption

The kinetic study of the adsorption process helps elucidate the rate-limiting step of the adsorption. In addition, an essential characteristic of a suitable adsorbent is fast adsorption kinetics. From a practical point of view, the efficiency of an adsorbent in an industrial process, such as adsorption in a fixed-bed column, as well as its capability to withstand the high flow rate of adsorbate gas, depends on its rate of adsorption. Hence, the study of adsorption kinetics is inherent to any adsorbent development strategy. As mentioned in
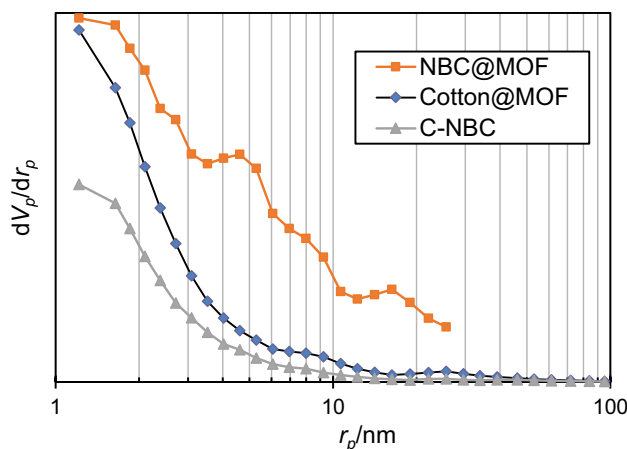
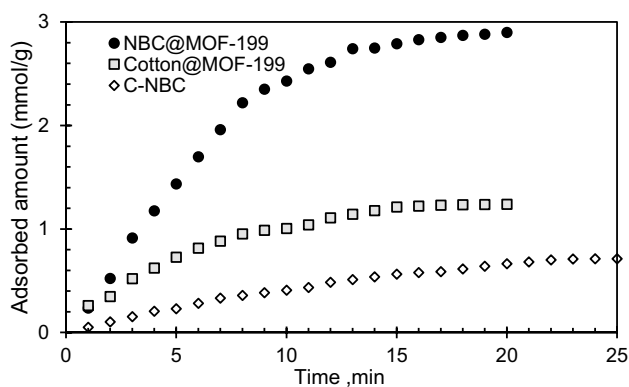**Fig. 6** BJH pore size distribution of samples

Fig. 7 CO_2 adsorption with time for C-NBC and the composites under ambient conditions

the experimental section, gravimetric adsorption tests were performed at various temperatures.

Figure 7 compares the CO_2 adsorption behavior of the C-NBC, NBC@MOF-199, and Cotton@MOF-199 composites at ambient temperature and pressure. The NBC@MOF-199 shows the highest final adsorption capacity (2.9 mmol g^{-1}), followed by Cotton@MOF-199 (1.2 mmol g^{-1}), and the C-NBC shows the lowest capacity of CO_2 adsorption (0.7 mmol g^{-1}). The adsorption of CO_2 onto cotton fabrics was negligible, and the results are not presented. It can be seen that the modification of NBC by growing the mesoporous MOF structure on its surface has increased the capacity of adsorption more than four times the C-NBC. These results align with surface area (a_{BET}) and micropore volume data obtained from the N_2 adsorption–desorption isotherms. The higher surface area provided by the mesoporous structure of MOF enhances the capability of the surface for the accommodation of CO_2 molecules.

In addition to providing higher surface are by the microporous structure of the MOF, the MOF-199 chemical

structure presents favorably active sites for CO_2 molecules to be attached. The HKUST-1 has been successfully reported as an adsorbent for CO_2 due to the great affinity of its open Cu(II) sites to CO_2 molecules [35]. Indeed, the presence of exposed metal ion sites in the structure of MOFs increases their functionality [34, 35]. The selective adsorption is facilitated by the presence of these active sites, since they have greater affinity with some molecules depending on their polarizability, dipole, or quadrupole moment [35]. $Cu_3(BTC)_2$(HKUST-1) is a good example of this kind of MOF. The number of favorable adsorption sites (coordinatively unsaturated metal centers) is higher and more uniformly distributed in the NBC@MOF-199 composite compared to the Cotton@MOF-199 due to better MOF coverage and higher density of nucleation sites for MOF growth.

Maximum CO_2 uptake at ambient temperature and pressure reported in literature for pure MOF-199, and various polysaccharide@MOF composite adsorbent systems are compared with the values obtained in this work in Table 2. The CO_2 uptake reported for pure MOF-199 (4.5 mmol g^{-1}) is higher than maximum value for NBC@MOF-199 composite (2.9 mmol g^{-1}) observed in the present study. In addition, the reported BET surface area of pure MOF-199 (~ 965) [46] is also higher than the surface area of NBC@MOF-199, i.e. ~ 553 cm^2 g^{-1}. It seems that some pores of the MOF are blocked by cotton/cellulose, anchoring sites or voids for CO_2 adsorption. It also must be noted that the reported adsorption capacity for the pure MOF is in mmol of adsorbate per gram of the MOF, whilst, in the composites it is in mmol per gram of composites, hence the lower adsorption capacities could be due to the concentration of MOF in the prepared composite. However, from practical point of view, the adsorption capacity per gram of the adsorbent system is the determining factor and it is decreased in the composites as compared to the pure MOF. Consequently, producing durable monoliths of MOF using cellulose substrate comes with the cost of loosing some adsorption sites, reducing the adsorption capacity. Comparing to other polysaccharide@MOF systems reported previously, the NBC@

MOF-199 of this study outperform them in terms of adsorption capacity at ambient temperature and pressure.

The process of adsorption in C-NBC and the composites was relatively short, and the equilibrium adsorption amount was reached in 20–30 min for all samples. The slope of the breakthrough curve is significantly higher in NBC@MOF-199 than the two other samples, which indicate that the process of adsorption was facilitated by the abundance of favorable adsorption active sites in this composite.

The adsorption kinetic data of the composites were further investigated by three kinetic models including pseudo-first order (PFO), Ritchie's n^{th} order (RNO), and the Weber and Morris (W&M) kinetic models. The selection of these models is because each model assumes a different rate-limiting step for adsorption kinetics. The PFO model considers the external or film diffusion as the rate-limiting step [49]. The RNO model is based on the assumption that the sorption to the active sites is the rate-limiting step [49]. Finally, the W&M model assumes that internal or intraparticle diffusion controls the adsorption rate [49]. The model that fits best to the kinetic data will determine the rate-limiting step of adsorption in this class of adsorbent composites.

Adsorption kinetic data for Cotton@MOF-199 composite and NBC@MOF-199 nanocomposite at three temperatures (RT, 45 °C, and 65 °C) were examined against different kinetic models. The details of the model parameters obtained from curve fitting and the correlation function associated with each curve fitting are available in the supporting information, Tables S1 and S2.

In all cases, the equilibrium adsorption capacity decreases with increasing adsorption temperature. For Cotton@MOF-199 composite (Fig. 8a,b, and c), at lower temperatures, both the PFO and RNO models show good performance to fit the kinetic data, with PFO showing a slightly higher correlation function of $R^2 = 0.995$ compared to the PSO model with $R^2 = 0.993$ (see supporting information, Table S2) for kinetic data at room temperature.

As the temperature increases, the correlation coefficient decreases for the external diffusion rate-limiting model (PFO) to $R^2 = 0.969$ at 45 °C, and $R^2 = 0.938$ at 65 °C. However, the kinetic models that consider the adsorption to the active sites as the rate-limiting step (Ritchie's n^{th} order) describe better the kinetics of adsorption as the adsorption temperature increases, with correlation functions of $R^2 = 0.984$ and $R^2 = 0.964$ at 45 and 65 °C, respectively (Table S1).

It seems that, at lower temperatures, the external diffusion (or film diffusion) governs the adsorption process with an essential contribution from adsorption to the active sites. As the temperature increases, the role of the sorption step to the active sites of the adsorption becomes more critical and controls the kinetics of adsorption. As mentioned previously, the active sorption sites in

Table 2 Maximum CO_2 uptake at ambient temperatures (25–30 C) and pressure reported in literature for polysaccharide@MOF systems

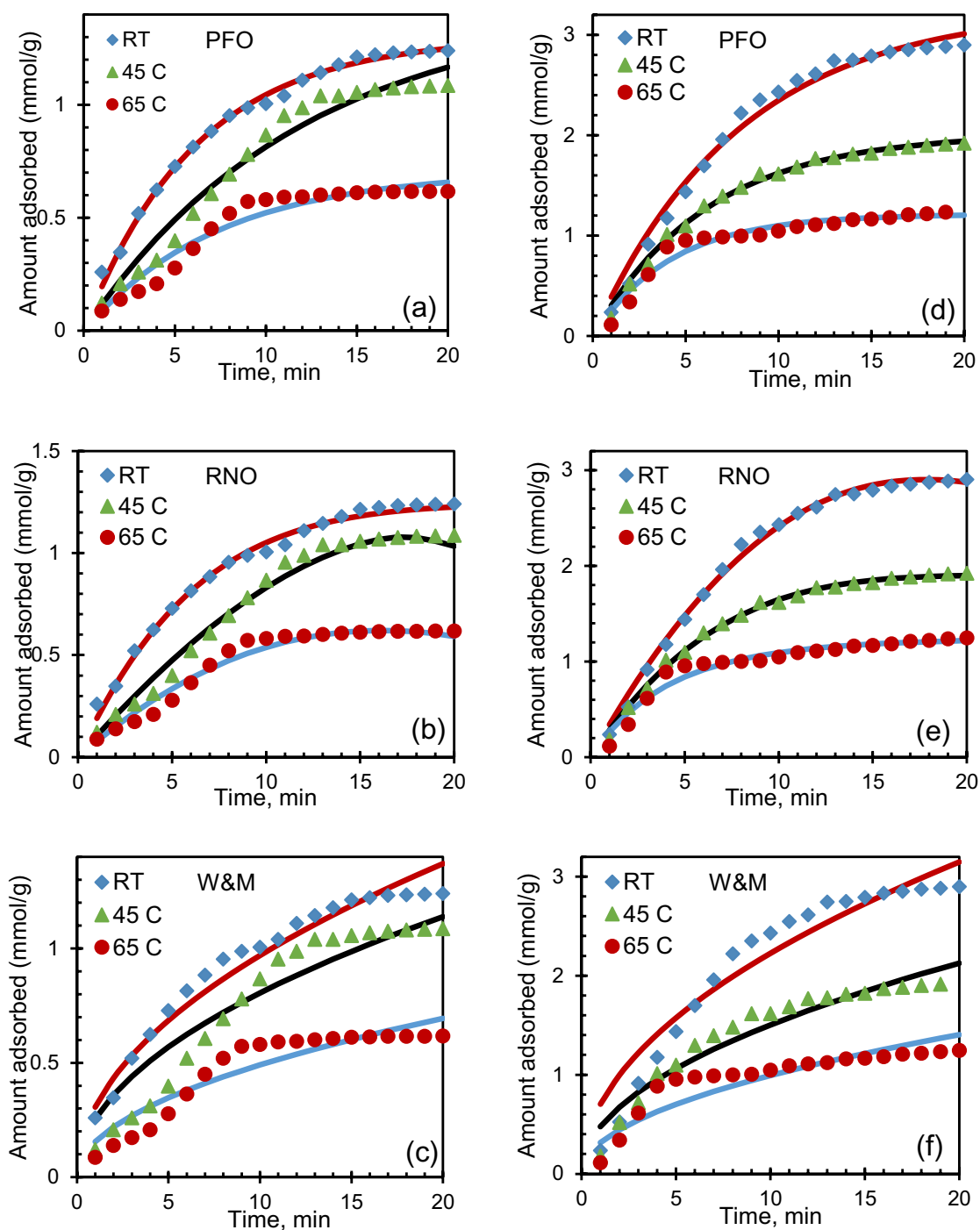| Adsorbent	Surface area (m^2 g^{-1})	CO$_2$ uptake (mmol g^{-1})	Ref
Pure MOF-199	964.5	4.5	[46]
Cyclodextrin (CD)-MOF(K$^+$)	400	0.55	[47]
NBC@NH$_2$-ZIF-8	455	1.63	[31]
TO-wood@MOF-199	471	1.46	[32]
CNF@ZIF-L	12	0.6	[48]
NBC@MOF-199	553.4	2.9	This work

Fig. 8 Fitting the kinetic data to PFO, RNO, and W&M models at different temperatures for Cotton@MOF-199 (**a**), (**b**), and (**c**) and for NBC@MOF-199 (**d**), (**e**), and (**f**)

MOF-199 are, in fact, the coordinatively unsaturated Cu^{2+} metal centers in the MOF-199 internal and external surfaces, which engage with the adsorbed CO_2 through physical interactions. It can be speculated that with a higher kinetic energy of CO_2 molecules at higher temperatures, the coordination of these molecules with the active metal centers slows down since the strength of this coordination becomes weaker at higher temperatures due to the higher mobility of CO_2 molecules.

The Weber and Morris kinetic model, which considers the intraparticle diffusion as the rate-limiting step, does not give a good fit to the experimental data of the Cotton@MOF-199

composites. Hence, the adsorption of CO_2 to the active sites is not restricted by the internal diffusion parameters.

A Similar behavior was observed in the case of NBC@MOF-199 as shown in Fig. 8d, e, and c. The Rithchie's n^{th}-order model performs well, specially at higher temperatures, and the W&M model shows the poorest fit at all temperatures. The sorption to active sites again controls the adsorption process of CO_2 molecules onto the composites. The kinetic behavior of the NBC@MOF-199 composites generally shows a higher correlation coefficient with all the kinetic models studied here, as compared to the kinetics of Cotton@MOF-199 composites. It could be due to more heterogeneous dispersion of MOF crystals on the cotton surface as well as the lower adsorption capacity of the cotton fabric substrates as compared to the NBC sheets. The lower equilibrium capacity of Cotton@MOF-199 compared to NBC@MOF-199 is due to the lower concentration of active metal centers in this composite, as discussed before.

Thermodynamics of CO_2 Adsorption

From the kinetic studies in the previous section, it seems that the NBC@MOF-199 nanocomposite is an interesting biocompatible adsorbent system that can be considered for CO_2 sequestration applications with relatively high adsorption capacity. For any newly developed adsorbent system, it is essential to investigate the spontaneity of the adsorption, exothermic/endothermic nature of adsorption, and the ease of CO_2 uptake and desorption for fast adsorption and low energy regeneration of adsorbent. These features can be investigated by thermodynamic parameters such as the Gibbs free energy change of adsorption, ΔG^0, the enthalpy change of adsorption, ΔH^0, and the activation energies for adsorption and desorption. In this section, we use adsorption and desorption kinetic data to estimate the thermodynamic parameters of the NBC@MOF-199 nanocomposite using the Langmuir kinetic model. As it was observed in the previous section, the adsorption is well described by models based on sorption to active sites; hence, the selection of the Langmuir model is appropriate for the discussion in this section.

The Langmuir kinetic model is expressed as [50]:

$$\frac{d\theta}{dt} = k_a C_o (1 - \theta) - k_d \theta \tag{1}$$

where θ is the fraction of surface coverage, k_a, C_o, and k_d are the rate constant for adsorption, concentration or partial pressure of CO_2 in the gas stream, and the desorption rate constant, respectively. At thermodynamic equilibrium, the rate of adsorption, $\frac{d\theta}{dt} = k_a C_o (1 - \theta)$, and desorption, $\frac{d\theta}{dt} = k_d \theta$, are equal. Considering that the relationship between fraction coverage, θ, the CO_2 uptake, $q(\frac{mmol}{g})$, and the maximum loading, $q_{max}(\frac{mmol}{g})$, can be expressed

as $q = q_{max}\theta$, one can integrate the adsorption and desorption rate equations to obtain:

$$q = q_{max}\left[1 - \exp\left(-k_a C_o t\right)\right] \tag{2}$$

$$q = q_{max} \exp\left(-k_d t\right) \tag{3}$$

The experimental data for adsorption and desorption can be fit to Eqs. 2 and 3 to determine k_a and k_d, and consequently, the adsorption equilibrium constant, $K_e = \frac{k_a}{k_d}$. The Gibbs free energy change of adsorption can be estimated by [51] :

$$\Delta G^0 = -RT \ln K_e \tag{4}$$

Considering the relationship between the ΔG^0, ΔH^0, and ΔS^0:

$$\Delta G^0 = \Delta H^0 - T\Delta S^0 \tag{5}$$

substituting from Eq. 4–4 into 4–5, we have:

$$\ln K_e = \frac{\Delta H^0}{RT} - \frac{\Delta S^0}{R} \tag{6}$$

Hence, by obtaining K_e at different temperatures and plotting $\ln K_e$ vs. $\frac{1}{T}$, we can estimate the enthalpy and entropy change of adsorption from the slope and intercept.

To estimate K_e at different temperatures, we need to obtain k_a and k_d from experimental adsorption and desorption kinetic data at various temperatures. For this reason, at the end of the adsorption kinetic experiments of NBC@MOF-199 at each temperature, presented in the previous section, the flow of CO_2 gas stream was stopped, and the system was purged with non-adsorbing He gas stream, and the desorption kinetics of the adsorbent was followed by recording the mass change of adsorbent with time. The results of the adsorption/desorption cycle are shown in Fig. 9.

The fittings of adsorption and desorption rate equations (Eqs. 2 and 3) are illustrated separately for the adsorption and desorption cycles in the supporting information, Fig. S1. The fitting parameters, the equilibrium constant, and the estimated Gibbs free energy change are summarized in Table 3. The estimated Gibbs free energy changes of CO_2 adsorption to the NBC@MOF-199 composite are − 1.68 kJ/mol, − 2.11 kJ/mol, and − 2.39 kJ/mol at RT(~ 25), 45 and 65 °C temperatures, respectively. The negative sign of free energy values (ΔG^0) indicates a spontaneous adsorption process.

The plot of $\ln K_e$ vs. $\frac{1}{T}$ is given in Fig. 10a. From the slope and intercept of the plot, the ΔH^0 and ΔS^0 are estimated − 3.6 kJ/mol and − 0.018 kJ/(mol. K), respectively. The negative change of enthalpy shows that the adsorption is exothermic, yet, the low absolute value of ΔH^0 is

Fig. 9 Adsorption and desorption kinetic data of CO_2 onto NBC@MOF-199 composites at three temperatures (RT(~ 25), 45 and 65 ℃). The vertical line shows the start of the desorption cycle
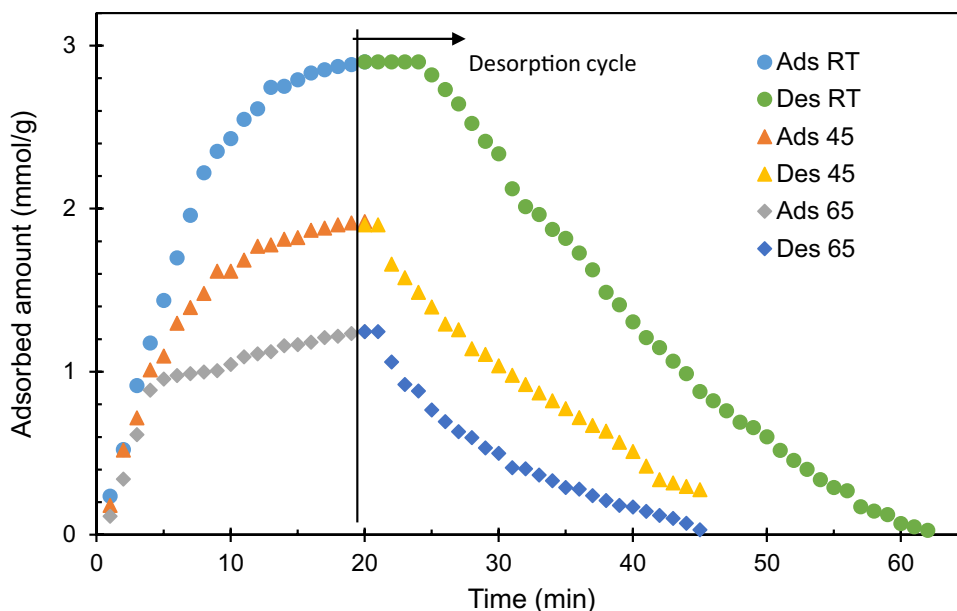

Table 3 Estimated adsorption and desorption rate constants, equilibrium coefficient, and free energy change of adsorption for NBC@MOF-199

Temperature	k_a	k_d	K_e	ΔG^0
RT ~ 25 °C	0.1265	0.0641	1.9735	− 1.68 kJ/mol
45 °C	0.1632	0.0734	2.2234	− 2.11 kJ/mol
65 °C	0.2377	0.1014	2.3442	− 2.39 kJ/mol

characteristic of a physisorption nature of the adsorption process in this system.

An important characteristic of an efficient adsorbent system is a high rate of adsorption and desorption that decreases the operational costs and energy requirements for regeneration of adsorbent. The activation energy of adsorption and desorption (E_a and E_d respectively) give important information about this characteristic of the adsorbent system.

They are related to the rate constants of adsorption and desorption via the Arrhenius equation:

$$k_a = A \exp\left(\frac{-E_a}{RT}\right) \& k_d = A \exp\left(\frac{-E_d}{RT}\right) \quad (7)$$

E_a and E_d can be estimated from the slope of $\ln k$ vs. $\frac{1}{T}$ as shown in Fig. 10b and c. The adsorption activation energy is estimated $E_a = 13.14$ kJ/mol, and for desorption $E_d = 9.51$ kJ/mol. The relatively low activation energies are characteristic of physisorption and represent fast rate adsorption and facilitated regeneration with low energy costs.

Antibacterial Activity of Composites

In addition to favorable adsorption behavior, as mentioned in the introduction section, the presented cellulose@MOF-199 composites are multifunctional and can find applications in solving many environmental related issues such as global warming, wastewater treatment, air purification, and medical masks and clothing. In fact, we studied the antibacterial activity of the developed cellulose@MOF-199 composites and they were very effective against both gram negative and gram positive bacteria.

In order to investigate the inhibitory effect of the cellulose@MOF-199, coagulase positive *Staphylococcus aureus* strain was used as an indicator of gram-positive bacteria and *Escherichia coli* strain was used as an indicator of gram-negative bacteria. These bacteria were inoculated in the culture medium and then the fabric with growth inhibitory properties was placed in the culture medium containing bacterial strain. After the incubation time, the tested plates were examined for growth halo and the results are as follows (Fig. 11):

- Diameter of non-growth halo of plate containing Escherichia coli strain (Fig. 11a): 33 mm.

- Diameter of non-growth halo of plate containing Staphylococcus aureus coagulase (Fig. 11b): 25 mm.

Conclusions

The emerging porous polysaccharide- metal–organic frameworks composites (polysaccharide@MOFs) are promising as efficient materials for CO_2 capture and separation. Herein we report the performance of two composite adsorbents
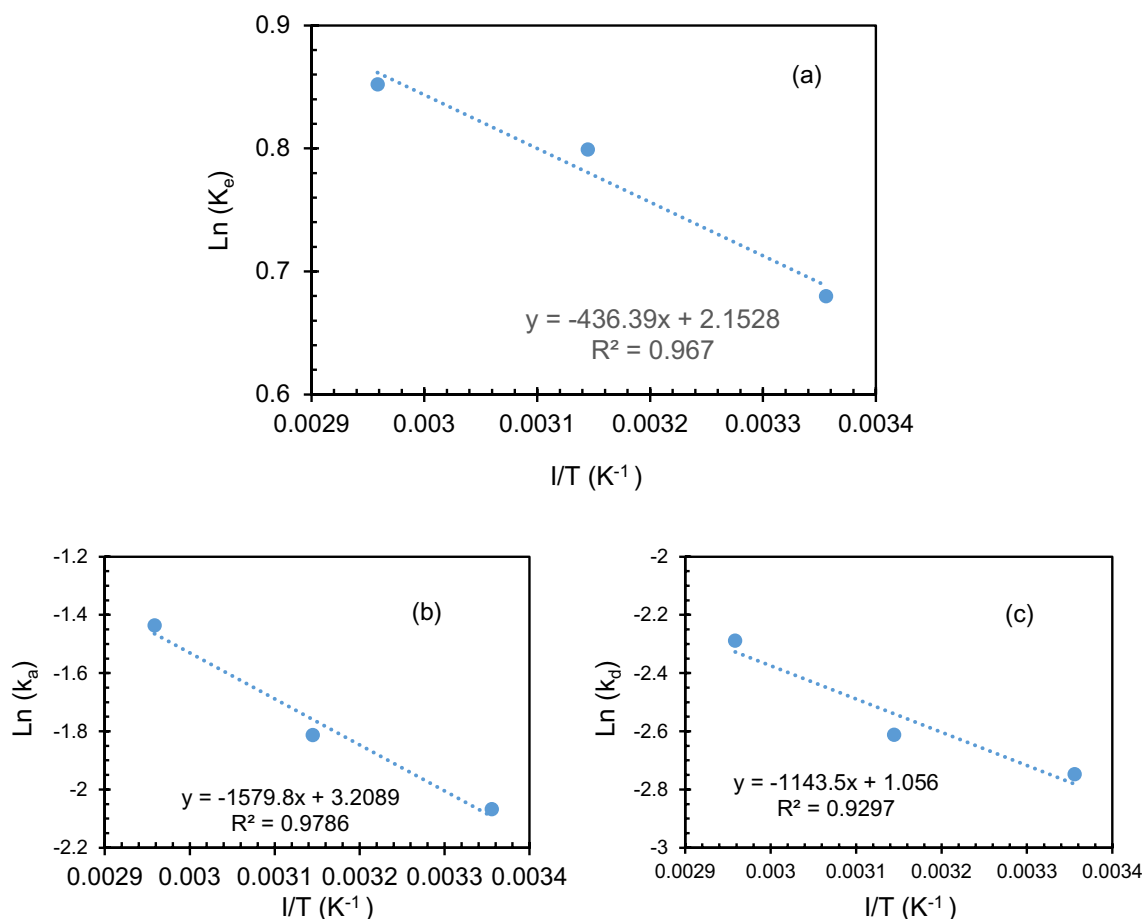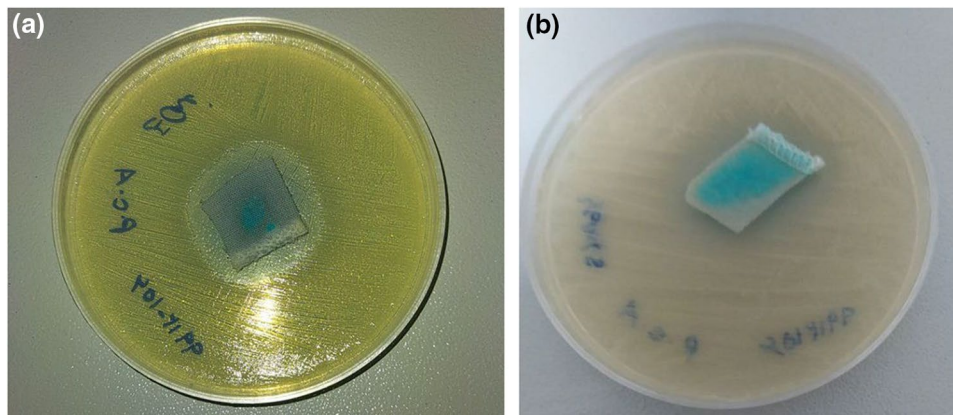
Fig. 10 The plot of **a** $\ln K_e$ vs. 1/T, **b** $\ln k_a$ vs 1/T and **c** $\ln k_d$ vs 1/T

Fig. 11 Antibacterial effect (growth inhibitory zone) of the cellulose@MOF-199 on **a** *Escherichia coli* and **b** *Staphylococcus aureus coagulase*

based on MOF-199 with bacterial cellulose nanofibers and cotton fabric as substrate, for CO_2 capture at ambient pressure. Bacterial cellulose and cotton fabrics provide efficient substrates to attach MOF-199 via chemical bonding permanently. The nanofiber network morphology of NBC provides a high surface area for introducing nucleation sites for MOF growth. Consequently, the higher degree of substitution of carboxylate groups, as favorable nucleation sites, are obtained during chemical modification as revealed by FTIR and SEM analysis. A maximum adsorption capacity of 2.9 mmol g^{-1} and 1.2 mmol g^{-1} for NBC@MOF-199 and Cotton@MOF-199, respectively. The abundance of active sorption sites, i.e., coordinatively unsaturated copper ion centers with strong interactions with CO_2 molecules, due

to complete coverage of MOF on NBC, is believed to be responsible for the high adsorption capacity NBC@MOF-199 composites. The kinetic study of CO_2 adsorption in the composites revealed that the mechanism of adsorption at lower temperatures is controlled by external diffusion and as the temperature increases, the adsorption to active sites becomes the rate-limiting step. Thermodynamic parameters of the adsorption process were reported for the interesting adsorbent system of NBC@MOF-199 via adsorption and desorption kinetic data. The negative sign of ΔG indicates spontaneous adsorption, and a small negative enthalpy change represents exothermic adsorption. The relatively low adsorption/desorption activation energies are characteristic of physisorption and represent fast rate adsorption and facilitated regeneration with low energy costs for this class of adsorbents, making them very desirable for commercialization.

Declarations

Conflict of interest The authors have no relevant financial or non-financial interests to disclose.

References

1. Millward AR, Yaghi OM (2005) Metal−organic frameworks with exceptionally high capacity for storage of carbon dioxide at room temperature. J Am Chem Soc 127:17998–17999

2. Simmons JM, Wu H, Zhou W, Yildirim T (2011) Carbon capture in metal–organic frameworks—a comparative study. Energy Environ Sci 4:2177–2185

3. Chung YG, Gómez-Gualdrón DA, Li P, Leperi KT, Deria P, Zhang H, Vermeulen NA, Stoddart JF, You F, Hupp JT (2016) In silico discovery of metal-organic frameworks for precombustion CO_2 capture using a genetic algorithm. Sci Ad 2:e1600909

4. Maurya M, Singh JK (2019) Effect of ionic liquid impregnation in highly water-stable metal-organic frameworks, covalent organic frameworks, and carbon-based adsorbents for post-combustion flue gas treatment. Energy Fuels 33:3421–3428

5. Furukawa S, Reboul J, Diring S, Sumida K, Kitagawa S (2014) Structuring of metal–organic frameworks at the mesoscopic/macroscopic scale. Chem Soc Rev 43:5700–5734

6. Chen Y, Wu J, Xiao J, Xi H, Xia Q, Li Z (2017) A new MOF-505@GO composite with high selectivity for CO_2/CH_4 and CO_2/N_2 separation. Chem Eng J 308:1065–1072

7. Prasanth KP, Rallapalli P, Raj MC, Bajaj HC, Jasra RV (2011) Enhanced hydrogen sorption in single walled carbon nanotube incorporated MIL-101 composite metal–organic framework. Int J Hydrogen Energy 36:7594–7601

8. Ameloot R, Liekens A, Alaerts L, Maes M, Galarneau A, Coq B, Desmet G, Sels BF, Denayer JFM, De Vos DE (2010) Silica–MOF composites as a stationary phase in liquid chromatography. Eur J Inorg Chem 2010:3735–3738

9. Somayajulu Rallapalli PB, Raj MC, Patil DV, Prasanth KP, Somani RS, Bajaj HC (2013) Activated carbon@ MIL-101 (Cr): a potential metal-organic framework composite material for hydrogen storage. Int J Energy Res 37:746–753

10. Hachemaoui M, Mokhtar A, Abdelkrim S, Ouargli-Saker R, Zaoui F, Hamacha R, Zahmani H, Hacini S, Bengueddach A, Boukoussa B (2021) Improved catalytic activity of composite beads calcium Alginate@ MIL-101@ Fe_3O_4 towards reduction toxic organic dyes. J Polym Environ 29:3813–3826

11. Kaur K, Jindal R, Tanwar R (2019) Chitosan–gelatin@ tin (IV) tungstatophosphate nanocomposite ion exchanger: synthesis, characterization and applications in environmental remediation. J Polym Environ 27:19–36

12. Zhu L, Zong L, Wu X, Li M, Wang H, You J, Li C (2018) Shapeable fibrous aerogels of metal–organic-frameworks templated with nanocellulose for rapid and large-capacity adsorption. ACS Nano 12:4462–4468

13. Ren W, Gao J, Lei C, Xie Y, Cai Y, Ni Q, Yao J (2018) Recyclable metal-organic framework/cellulose aerogels for activating peroxymonosulfate to degrade organic pollutants. Chem Eng J 349:766–774

14. Zhang XF, Feng Y, Wang Z, Jia M, Yao J (2018) Fabrication of cellulose nanofibrils/UiO-66-NH_2 composite membrane for CO_2/N_2 separation. J Membr Sci 568:10–16

15. Lei C, Gao J, Ren W, Xie Y, Abdalkarim SYH, Wang S, Ni Q, Yao J (2019) Fabrication of metal-organic frameworks@ cellulose aerogels composite materials for removal of heavy metal ions in water. Carbohydr Polym 205:35–41

16. Sun L, Shen J, An X, Qian X (2021) Fire retardant, UV and blue light double-blocking super clear Carboxymethylated cellulose bioplastics enabled by metal organic framework. Carbohydr Polym 273:118535

17. Duan C, Meng J, Wang X, Meng X, Sun X, Xu Y, Zhao W, Ni Y (2018) Synthesis of novel cellulose-based antibacterial composites of Ag nanoparticles@ metal-organic frameworks@ carboxymethylated fibers. Carbohydr polym 193:82–88

18. Ma X, Lou Y, Chen XB, Shi Z, Xu Y (2019) Multifunctional flexible composite aerogels constructed through in-situ growth of metal-organic framework nanoparticles on bacterial cellulose. Chem Eng J 356:227–235

19. Qian L, Lei D, Duan X, Zhang S, Song W, Hou C, Tang R (2018) Design and preparation of metal-organic framework papers with enhanced mechanical properties and good antibacterial capacity. Carbohydr polym 192:44–51

20. Liu Q, Yu H, Zeng F, Li X, Sun J, Li C, Lin H, Su Z (2021) HKUST-1 modified ultrastability cellulose/chitosan composite aerogel for highly efficient removal of methylene blue. Carbohydr polym 255:117402

21. Lu W, Duan C, Liu C, Zhang Y, Meng X, Dai L, Wang W, Yu H, Ni Y (2020) A self-cleaning and photocatalytic cellulose-fiber-supported "Ag@ AgCl@ MOF-cloth''membrane for complex wastewater remediation. Carbohydr Polym 247:116691

22. Nie J, Xie H, Zhang M, Liang J, Nie S, Han W (2020) Effective and facile fabrication of MOFs/cellulose composite paper for air

hazards removal by virtue of in situ synthesis of MOFs/chitosan hydrogel. Carbohydr polym 250:116955

23. Abdelhameed RM, Rehan M, Emam HE (2018) Figuration of Zr-based MOF@ cotton fabric composite for potential kidney application. Carbohydr polym 195:460–467

24. Javanbakht S, Pooresmaeil M, Namazi H (2019) Green one-pot synthesis of carboxymethylcellulose/Zn-based metal-organic framework/graphene oxide bio-nanocomposite as a nanocarrier for drug delivery system. Carbohydr polym 208:294–301

25. Abdelhamid HN, Mathew AP (2022) Cellulose–metal organic frameworks (CelloMOFs) hybrid materials and their multifaceted applications: a review. Coord Chem Rev 451:214263

26. Abdelhamid HN, Mathew AP (2021) Cellulose-zeolitic imidazolate frameworks (CelloZIFs) for multifunctional environmental remediation: Adsorption and catalytic degradation. Chem Eng J 426:131733

27. Jia M, Zhang XF, Feng Y, Zhou Y, Yao J (2020) In-situ growing ZIF-8 on cellulose nanofibers to form gas separation membrane for CO_2 separation. J Membr Sci 595:117579

28. Policicchio A, Florent M, Attia MF, Whitehead DC, Jagiello J, Bandosz TJ (2020) Effect of the incorporation of functionalized cellulose nanocrystals into UiO-66 on composite porosity and surface heterogeneity alterations. Adv Mater Interfaces 7:1902098

29. Mubashir M, Dumée LF, Fong YY, Jusoh N, Lukose J, Chai WS, Show PL (2021) Cellulose acetate-based membranes by interfacial engineering and integration of ZIF-62 glass nanoparticles for CO_2 separation. J Hazard Mater 415:125639

30. Raza A, Japip S, Liang CZ, Farrukh S, Hussain A, Chung TS (2021) Novel cellulose triacetate (CTA)/cellulose diacetate (CDA) blend membranes enhanced by amine functionalized ZIF-8 for CO_2 separation. Polymers 13(17):2946

31. Ma H, Wang Z, Zhang XF, Ding M, Yao J (2021) In situ growth of amino-functionalized ZIF-8 on bacterial cellulose foams for enhanced CO_2 adsorption. Carbohydr Polym 270:118376

32. Wang S, Wang C, Zhou Q (2021) Strong foam-like composites from highly mesoporous wood and metal-organic frameworks for efficient CO_2 capture. ACS Appl Mater Interfaces 13:29949–29959

33. Al-Janabi N, Hill P, Torrente-Murciano L, Garforth A, Gorgojo P, Siperstein F, Fan X (2015) Mapping the Cu-BTC metal–organic framework (HKUST-1) stability envelope in the presence of water vapour for CO_2 adsorption from flue gases. Chem Eng J 281:669–677

34. Van Assche TR, Duerinck T, Van der Perre S, Baron GV, Denayer JF (2014) Prediction of molecular separation of polar–apolar mixtures on heterogeneous metal–organic frameworks: HKUST-1. Langmuir 30:7878–7883

35. Ongari D, Tiana D, Stoneburner SJ, Gagliardi L, Smit B (2017) Origin of the strong interaction between polar molecules and copper (II) paddle-wheels in metal organic frameworks. J Phys Chem 121:15135–15144

36. Chowdhury P, Mekala S, Dreisbach F, Gumma S (2012) Adsorption of CO, CO_2 and CH_4 on Cu-BTC and MIL-101 metal organic frameworks: Effect of open metal sites and adsorbate polarity. Microporous Mesoporous Mater 152:246–252

37. Liang Z, Marshall M, Chaffee AL (2009) CO_2 adsorption-based separation by metal organic framework (Cu-BTC) versus zeolite (13X). Energy Fuels 23:2785–2789

38. Lange LE, Obendorf SK (2015) Functionalization of cotton fiber by partial etherification and self-assembly of polyoxometalate encapsulated in $Cu_3(BTC)_2$ metal–organic framework. ACS Appl Mater Interfaces 7:3974–3980

39. Wang JY, Mangano E, Brandani S, Ruthven DM (2021) A review of common practices in gravimetric and volumetric adsorption kinetic experiments. Adsorption 27:295–318

40. Tomé LC, Freire MG, Rebelo LPN, Silvestre AJ, Neto CP, Marrucho IM, Freire CS (2011) Surface hydrophobization of bacterial and vegetable cellulose fibers using ionic liquids as solvent media and catalysts. Green Chem 13:2464–2470

41. Wada M, Okano T, Sugiyama J (2001) Allomorphs of native crystalline cellulose I evaluated by two equatorial d-spacings. J Wood Sci 47:124–128

42. Schlichte K, Kratzke T, Kaskel S (2004) Improved synthesis, thermal stability and catalytic properties of the metal-organic framework compound $Cu_3(BTC)_2$. Microporous Mesoporous Mater 73:81–88

43. Kondor A, Santmarti A, Mautner A, Williams D, Bismarck A, Lee KY (2021) On the BET surface area of nanocellulose determined using volumetric, gravimetric and chromatographic adsorption methods. Front Chem Eng 3:738995

44. Oshima T, Taguchi S, Ohe K, Baba Y (2011) Phosphorylated bacterial cellulose for adsorption of proteins. Carbohydr Polym 83:953–958

45. Thommes M, Kaneko K, Neimark AV, Olivier JP, Rodriguez-Reinoso F, Rouquerol J, Sing KS (2015) Physisorption of gases, with special reference to the evaluation of surface area and pore size distribution (IUPAC Technical Report). Pure Appl Chem 87:1051–1069

46. Wang QM, Shen D, Bülow M, Lau ML, Deng S, Fitch FR, Lemcoff NO, Semanscin J (2002) Metallo-organic molecular sieve for gas separation and purification. Microporous Mesoporous Mater 55:217–230

47. Yan TK, Nagai A, Michida W, Kusakabe K, Yusup S (2016) Crystal growth of cyclodextrin-based metal-organic framework for carbon dioxide capture and separation. Proc Eng 148:30–34

48. Valencia L, Abdelhamid HN (2019) Nanocellulose leaf-like zeolitic imidazolate framework (ZIF-L) foams for selective capture of carbon dioxide. Carbohydr polym 213:338–345

49. Wang J, Guo X (2020) Adsorption kinetic models: physical meanings, applications, and solving methods. J Hazard Mater 390:122156

50. Mathias PM, Kumar R, Moyer JD, Schork JM, Srinivasan SR, Auvil SR, Talu O (1996) Correlation of multicomponent gas adsorption by the dual-site Langmuir model. Application to nitrogen/oxygen adsorption on 5A-zeolite. Ind Eng Chem Res 35:2477–2483

51. Ko YG, Shin SS, Choi US (2011) Primary, secondary, and tertiary amines for CO_2 capture: designing for mesoporous CO_2 adsorbents. J Colloid Interface Sci 361:594–602